arXiv:1809.10582v1 [cs.CV] 27 Sep 2018

Kernel Based Low-Rank Sparse Model for Single Image Super-Resolution

Jiahe Shi*, Chun Qi*

School of Electronic and Information Engineering,Xi'an Jiaotong University

Xi'an, Shaanxi 710049 China

Abstract

Self-similarity learning has been recognized as a promising method for single image super-resolution (SR) to produce high-resolution (HR) image in recent years. The performance of learning based SR reconstruction, however, highly depends on learned representation coefficients. Due to the degradation of input image, conventional sparse coding is prone to produce unfaithful representation coefficients. To this end, we propose a novel kernel based low-rank sparse model with self-similarity learning for single image SR which incorporates nonlocal-similarity prior to enforce similar patches having similar representation weights. We perform a gradual magnification scheme, using self-examples extracted from the degraded input image and up-scaled versions. To exploit nonlocal-similarity, we concatenate the vectorized input patch and its nonlocal neighbors at different locations into a data matrix which consists of similar components. Then we map the nonlocal data matrix into a high-dimensional feature space by kernel method to capture their nonlinear structures. Under the assumption that the sparse coefficients for the nonlocal data in the kernel space should be low-rank, we impose low-rank constraint on sparse coding to share similarities among representation coefficients and remove outliers in order that stable weights for SR

☆This research is supported by the National Natural Science Foundation of China grant numbers [61572395, 61601362, 61133008].

*Corresponding author

Email addresses: sjh19900831@163.com (Jiahe Shi), qichun@mail.xjtu.edu.cn (Chun Qi)

reconstruction can be obtained. Experimental results demonstrate the advantage of our proposed method in both visual quality and reconstruction error.
Keywords: low-rank, sparse representation, kernel method, self-similarity learning, super-resolution

---

1. Introduction

High resolution (HR) images are generally preferred to low resolution (LR) ones in many applications of computer vision, such as remote sensing, medical imaging and video surveillance. However, the resolution is always limited by the constraint of optical imaging systems and hardware devices. As a software technique to break this limitation, super-resolution (SR) has been developed to reconstruct HR images from the observed LR ones using specific algorithms. SR methods can be divided into two categories: reconstruction based and learning based methods.

Reconstruction based methods recover HR images with help of prior knowledge and statistics of natural images, such as gradient profile prior [1], Gaussian mixture model [2], wavelet based model [3] and total variation (TV) [4]. Global constraint [5] has also been widely used as a typical back-projection technique for SR.

Learning based methods predict the missing HR details by learning the model of relationships between pairs of LR and HR examples. The representative methods include neighbor embedding (NE) algorithm [6], sparse coding (SC) based method [7] and position-based method [8]. As for the above mentioned learning based methods, external examples from training images are required.

However, internal examples instead of external ones can also be utilized. In nature images, sufficient examples which are highly correlated to the input patches can be found in the input image, its repeatedly down-sampled and subsequently up-scaled versions. In the past few years, self-similarity has been successfully utilized for SR[9, 10, 11, 12]. Glasner et al. [9] first designed an ap-

pealing self-similarity learning framework. With the help of self-examples, the input image is repeatedly magnified to the desired size. By this coarse-to-fine strategy, the difficulty of each step is alleviated, which benefits the performance of the whole SR system. Due to these advantages, self-similarity learning has been followed by many researchers in recent years. Bevilacqua et. al [12] proposed a new double pyramid SR model with simple multi-variate regression to learn the direct mappings between LR and HR patches. Zhang et. al [10] presented a neighbor embedding based self-similarity learning SR scheme with spatially nonlocal regularization. Yu et. al [11] combined the self-similarity learning with sparse representation to perform SR. However, due to the degradation (i.e. blurring and down-sampling) of the observed image which is also the source of self-examples. The above mentioned conventional learning methods are prone to produce unfaithful representation coefficients, which are not suitable for accurate SR reconstruction. To solve the problem, a nonlocally constrained learning methods have been introduced recently [13]. Dong et. al [13] proposed a nonlocally centralized sparse representation for image restoration using PCA dictionary trained from self-examples. Specifically, they defined the deviation of the learned sparse codes from the expected true ones as sparse coding noise (SCN). As suggested by their work, SR performance can be improved by suppressing SCN through calculating nonlocal means of the sparse codes for similar neighbors of the LR input patches as an estimation of the optimal codes. However, the estimation is still a weighted linear combination of codes for the similar patches. In our previous work[14], we found that nonlinear low-rank constraint can be used to suppress SCN in self-similarity learning scheme for SR. Furthermore, in this paper, we propose a novel kernel based low-rank sparse coding (KLRSC) method via self-similarity learning for single image SR. Self-examples are extracted from the input image itself, its degraded versions and up-scaled ones. The input image is gradually super-resolved. In each magnification, similar column components of a nonlocal data matrix which consists of a vectorized input patch and its nonlocal neighbors can be observed. This property of similarity leads to the nature of low-rank. Furthermore, we also

use the kernel method [15] to capture nonlinear structures of data, the nonlocal data are mapped into a high-dimensional feature space by kernel method. In our work, we find that the low-rank property is preserved when the nonlocal patches are mapped into the kernel space. Due to this observation, we assume that the sparse codes for nonlocal matrices should be approximately low-rank. Thus, we perform kernel based low-rank sparse coding to gain accurate coefficients for self-similarity learning based SR. Experimental results demonstrate the advantage of our proposed method in both visual quality and reconstruction error. Our contributions are two folds:

1. The low-rank property is proved to be preserved when the nonlocal data are mapped into high dimensional space by kernel method.
2. A novel kernel based low-rank sparse coding based scheme for single image SR is proposed, which exploits both low-rank property and nonlinear structural information of nonlocal data in a high-dimensional space.

The remainder of this paper is organized as follows. In Section 2, we describe the proposed method in detail. The experimental results are given in Section 3. We conclude this paper in Section 4.

Our preliminary work has appeared in [14].

2. Proposed kernel based low-rank sparse model for single image SR

2.1. Overview

In this section, we start the discussion of the kernel based low-rank sparse model for single image SR. We adopt the double pyramid self-similarity learning framework which is the same as that of [12]. By coarse-to-fine strategy, the observed image is zoomed in by several times to reach the expected size. In each magnification, we perform KLRSC to learn the representation coefficients for SR reconstruction. Both the self-examples, the structural information and the underlying nonlinear structure of nonlocal similar examples are exploited in

the coding stage. Then, an interim image can be recovered by the learned coefficients and self-examples for the next magnification. When the image reaches the desired size, the iterations of magnification will terminate.

2.2. Self-similarity learning and gradual magnification

In the stage of self-similarity learning, the pairs of examples are extracted from two pyramids of images. The flowchart of the double pyramids model is shown in Fig. 1. We denote the pyramid which composes of the sequences of the input image and its several down-sampled versions as I_{-n} for $n = 1, 2, ...N_D$. Given the input image I_0, the down-sampling is repeated for N_D times with a factor of $s = 1.25$ at each time. The n-th layer I_{-n} is represented as:

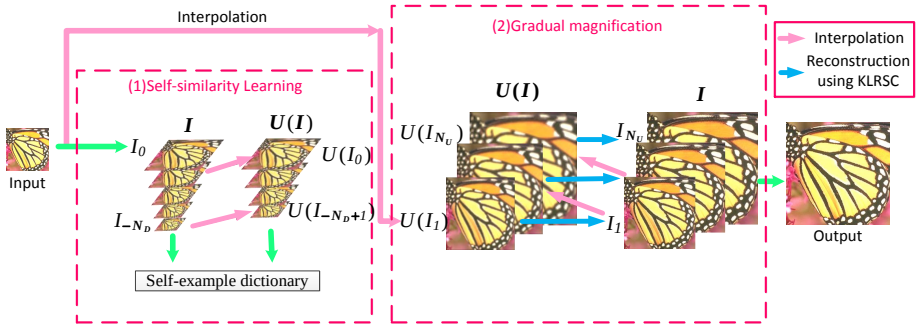

Figure 1: Overview of double pyramids model for single image SR. Sub-figure (1) with dashed lines stands for collection of self-examples . Sub-figure (2) with dashed lines denotes the gradual magnification with KLRSC for SR reconstruction.

$$I_{-n} = (I_0 * B_n)_{\downarrow s^n} \tag{1}$$

where $*$ is a convolution operator and $\downarrow s^n$ denotes the down-sampling operator by a factor of s^n. B_n is a Gaussian blur kernel with a standard variance σ_n^2 which can be computed as [16]:

$$\sigma_n^2 = n\sigma^2 log(s)/log(p) \tag{2}$$

The up-scaled pyramid $U(I_{-n})$ by bicubic interpolation is established as:

$$U(I_{-n}) = (I_{-n-1})_{\uparrow s} \tag{3}$$

where $U(I_{-n})$ is the n-th layer of the up-scaled pyramid with respect to the layer I_{-n} and $\uparrow s$ is an up-scaling operator by a factor of s. In order to obtain the pairs of self-examples, layer I_{-n} and the corresponding layer $U(I_{-n})$ are divided into overlapping patches. For each patch from $U(I_{-n})$, we use four high-pass filters to extract its gradient feature of the first- and second-order gradients in both vertical and horizontal directions:

$$f_1 = [1, -1], f_2 = {f_1}^T, f_3 = [-1, 2, -1], f_4 = {f_3}^T. \tag{4}$$

The four high-pass filtered features are concatenated into vector as a descriptor of the patch. As for the corresponding patch from I_{-n}, we extract its intensity feature by subtracting its mean value. We collect these two kinds of features from all layers and normalize them to unit $\ell 2$-norm to construct the dictionary. Let $H = \{x_r^d\}_{r=1}^K \in \mathbb{R}^{b \times K}$ represent the dictionary for reconstruction and $L = \{y_r^d\}_{r=1}^K \in \mathbb{R}^{4b \times K}$ denote the one for learning.

In multi-step magnification, we gradually super-resolve the input image I_0. Given the total up-scale factor p, we repeat the magnification for $N_U = ceil(log_s p)$ times, where $ceil(x)$ returns the nearest integer larger than x. In the i-th magnification for $i = 1, 2, ...N_U$, we produce the interim layer by:

$$U(I_i) = (I_{i-1})_{\uparrow s} \tag{5}$$

Then we partition the i-th layer $U(I_i)$ is into overlapped patches and convert them into a set of normalized gradient features $Y^i = \{y_j\}_i$. We recover the corresponding patches $X_i = \{x_j\}_i$ by kernel based low-rank sparse representation and reconstruct the layer I_i by weighted average operation on the overlapped region, which we describe in the following subsection.

2.3. Kernel based low-rank sparse representation for SR reconstruction

In this subsection, we present how to recover the super-resolved layers from the interpolated ones using our proposed KLRSC. We first describe the algorithm of KLRSC for SR reconstruction. Then we present the post-processing

procedure by the incorporation of iterative back projection (IBP) [5] and pixel-wise autoregressive (AR) model regularization [17] to improve the quality of reconstructed layer.

Fig. 2 gives the illustration of KLRSC for SR reconstruction. Nonlocal-similarity is an effective prior for image reconstruction [10, 11, 13, 18, 19, 20], which means that small patches tend to appear repeatedly at different locations of a natural image. For each j-th feature vector y_j extracted from the i-th layer $U(I_i)$, we select its K_N most similar nonlocal neighbors in the same layer and stack them as columns $Y_j^N = \{y_t\}_{t \in G_N(j)} \in \mathbb{R}^{4b \times K_N}$ where $G_N(j)$ refers to the indices of the nonlocal data. We also find its K_D nearest atoms in the dictionary L to create an subset $Y_j^D = \{y_r^d\}_{r \in G_D(j)} \in \mathbb{R}^{4b \times K_D}$ for learning and accumulate the corresponding atoms in the dictionary H to form the subset $X_j^D = \{x_r\}_{r \in G_D(j)} \in \mathbb{R}^{b \times K_D}$ for reconstruction. $G_d(j)$ denotes the indices of the selected atoms.

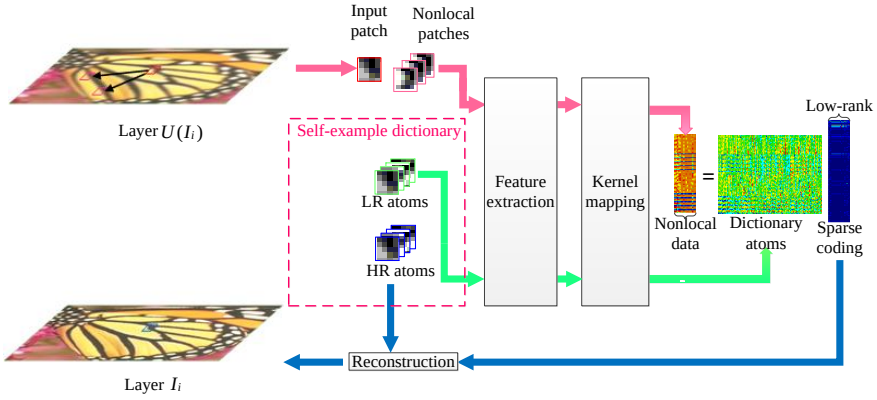

Figure 2: KLRSC method for SR reconstruction.

2.3.1. Implementation of KLRSC for SR

In standard sparse coding, the sparse coding for the feature vector y_j can be formulated as:

$$w = \arg\min_{\alpha} \frac{1}{2}||y_j - Y_j^D w||_2^2 + \lambda||w||_1 \tag{6}$$

Different from the conventional approach, Recently, Zhang et. al [21] proposed a low-rank sparse coding method for image classification. They encoded densely sampled SIFT features in spatially local domain. The codes for spatially local features were assumed to be low-rank. we introduce a low-rank constraint to regularize the representations for similar feature vectors. We attach the feature vector y_j to the nonlocal feature vectors Y_j^N to combine a grouped matrix $Y_j^A = [y_j, Y_j^N]$ with the nature of low-rank property. The corresponding sparse coefficient matrix for representing the data upon the subset Y_j^D is also expected to be low-rank. Low-rank optimization relies on the proof that the convex envelope of rank is the nuclear norm under broad conditions [22]. Based on this theorem, low-rank optimization has been successfully used in many applications [23, 24, 25, 26, 27, 28] We use nuclear norm constraint [22] to formulate the low-rank optimization. The augmented optimization problem can be written as:

$$W_j = \underset{W_j}{\operatorname{argmin}} \frac{1}{2}||Y_j^A - Y_j^D W_j||_{\mathrm{F}}^2 + \lambda_1||W_j||_1 + \lambda_2||W_j||_* \tag{7}$$

where W_j represents the corresponding weights that each atom in the subset Y_j^D contributes in the reconstruction of the augmented data Y_j^A. The nuclear norm $||\cdot||_*$ is calculated by the sum of the matrix singular values, which is an approximation of rank. λ_1 and λ_2 are the parameters balancing different regularization terms.

We also use the kernel method [15] to capture the nonlinear structures of features, which can reduce the feature quantization error and improve the coding performance. As suggested by [29, 30], we transform the augmented data Y_j^A and the LR subset Y_j^D into high dimensional space by the nonlinear mapping: $\phi : R^{4b} \rightarrow R^F (4b << F)$ to capture the relationship between them. The augmented features are transformed to $\phi(Y_j^A)$ and the corresponding LR subset is mapped to $\phi(Y_j^D)$. Given two column features x and y, we define a kernel function $k(x, y) = \phi(x)^T \phi(y)$. In our work, we use Gaussian kernel function $k(x, y) = exp(-||x - y||_2^2/\sigma_G^2)(\sigma_G = 1)$. Thus the kernel matrix $\phi(Y_j^D)^T \phi(Y_j^A)$ can be represented as $K_{Y_j^D Y_j^A}$ where the element $(K_{Y_j^D Y_j^A})_{m,n} = k(y_{j,m}^D, y_{j,n}^A)$.

In Fig. 3, we draw the nuclear norm distributions of the nonlocal matrices consisting of nonlinearly mapped nonlocal feature vectors. The feature vectors extracted from a test image and their 20 nonlocal neighbors are concatenated to form matrices of nonlocal features. Note that the nuclear norm of nonlinear mapped nonlocal matrix $\phi(Y)$ is calculated as $||\phi(Y)||_* = tr(\Sigma(\phi(Y)^T\phi(Y))) = tr(\Sigma(K_{Y,Y}))$ where $\Sigma(K_{Y,Y})$ denotes the diagonal matrix with the eigenvalues of $K_{Y,Y}$ on the diagonal and $tr(\cdot)$ is the matrix trace operator. It shows that the matrices of nonlocal features tend to have relatively lower nuclear norms than their maximum (21), which indicates the low-rank property of nonlocal matrices.

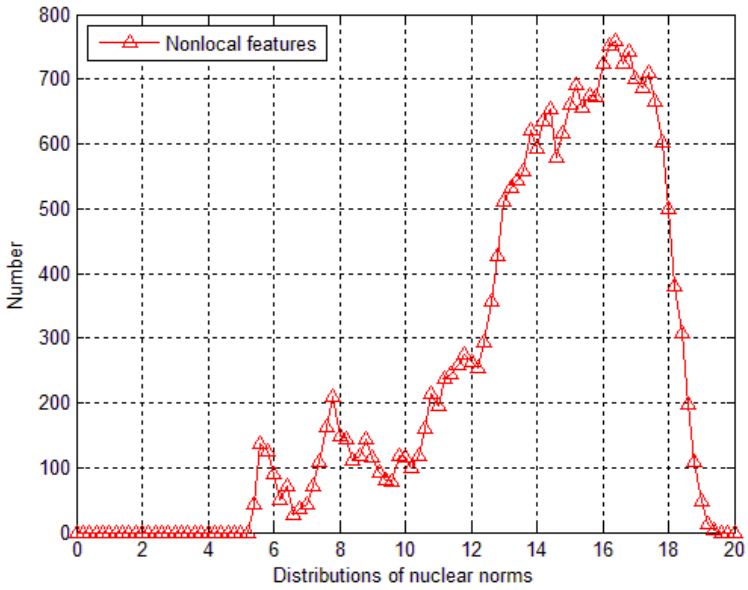

Figure 3: Nuclear norm distributions of the matrices consisting of nonlinearly mapped nonlocal feature vectors. The feature vectors and their nonlocal neighbors are concatenated to form matrices of nonlocal features.

Thus, with this preservation of low-rank property, the optimization problem of (7) in kernel space can be rewritten as:

$$W_j = \underset{W_j}{\operatorname{argmin}} \frac{1}{2}||\phi(Y_j^A) - \phi(Y_j^D)W_j||_{\mathrm{F}}^2 + \lambda_1||W_j||_1 + \lambda_2||W_j||_* \qquad (8)$$

However, since the optimization problems of nuclear norm and $\ell 1$ norm (8) are difficult to solve simultaneously, we introduce two more relaxation variables and impose fidelity constraints between the pairs of relaxation variables:

$$W_{1\sim 3,j} = \underset{W_{1\sim 3,j}}{\operatorname{argmin}} \frac{1}{2}||\phi(Y_j^A) - \phi(Y_j^D)W_{3,j}||_{\mathrm{F}}^2 + \lambda_1||W_{1,j}||_1 + \lambda_2||W_{2,j}||_*,$$
$$\text{s.t.} W_{3,j} = W_{1,j}; W_{3,j} = W_{2,j} \quad (9)$$

We use inexact augmented Lagrange multiplier (IALM) method [31] to solve problem (9), which has also been used to efficiently solve other low-rank problems (i.e. RPCA for low rank matrix recovery [23]). We add two more variables to relax the fidelity constraints. The augmented Lagrange function for (9) is:

$$\begin{aligned} L(W_{1\sim 3,j}) = \frac{1}{2}||\phi(Y_j^A) - \phi(Y_j^D)W_{3,j}||_{\mathrm{F}}^2 + \lambda_1||W_{1,j}||_1 + \lambda_2||W_{2,j}||_* \\ + tr(\Lambda_1^T(W_{1,j} - W_{3,j})) + tr(\Lambda_2^T(W_{2,j} - W_{3,j})) \\ + \frac{\mathrm{u}_1}{2}||W_{1,j} - W_{3,j}||_{\mathrm{F}}^2 + \frac{\mathrm{u}_2}{2}||W_{2,j} - W_{3,j}||_{\mathrm{F}}^2 \quad (10) \end{aligned}$$

where $tr(\cdot)$ is the operator to get matrix trace. λ_1 and λ_2 are scalar constants. Λ_1 and Λ_2 are Lagrange multiplier matrices. u_1 and u_2 are the parameters balancing the difference between pairs of objective variables and other regularization terms.

2.3.2. Optimization of KLRSC

There are three objective variables $W_{1\sim 3,j}$ in (10) which we alternatively update, followed by the adjustment of multipliers. Soft-threshold operations on matrix elements and singular values are used to solve the problem of $\ell 1$-norm and nuclear norm optimizations. The update steps of $W_{1\sim 3,j}$ and the multipliers are given below.

Update $W_{1,j}$

Firstly, we update $W_{1,j}$ and meanwhile fix other variables. The optimization function with respect to $W_{1,j}$ derived from (10) can be formulated as:

$$\arg\min_{W_{1,j}} \frac{\lambda_1}{u_1}||W_{1,j}||_1 + \frac{1}{2}||W_{1,j} - (W_{3,j} + \frac{1}{u_1}\Lambda_1)||_F^2 \quad (11)$$

The $\ell 1$-norm optimization problem of (11) can be solved by soft-thresholding:

$$W_{1,j} = S_{\frac{\lambda_1}{u_1}}(W_{3,j} + \frac{1}{u_1}\Lambda_1) \tag{12}$$

where $S_\lambda(W)$ =sign(W)max$(0, |W| - \lambda)$ is a shrinkage operator on values of matrix W.

Update $W_{2,j}$

Then we update $W_{2,j}$ and fix others by solving the following optimization problem:

$$\arg\min_{W_{2,j}} \frac{\lambda_2}{u_2}||W_{2,j}||_* + \frac{1}{2}||W_{2,j} - (W_{3,j} + \frac{1}{u_2}\Lambda_2)||_F^2 \tag{13}$$

The nuclear norm optimization problem of (13) can be solved by singular value soft-thresholding:

$$W_{2,j} = \Im_{\frac{\lambda_2}{u_2}}(W_{3,j} + \frac{1}{u_2}\Lambda_2) \tag{14}$$

where $\Im_\lambda(W) = U_W S_\lambda(\Sigma_W)V_W^T$ is a shrinkage operator on singular values of matrix W and $U_W\Sigma_W V_W^T$ is the singular value decomposition of W.

Update $W_{3,j}$

The optimization function with respect to $W_{3,j}$ is given by:

$$\begin{aligned}\arg\min_{W_{3,j}} &\frac{1}{2}||\phi(Y_j^A) - \phi(Y_j^D)W_{3,j}||_{\mathrm{F}}^2 + tr(\Lambda_1^T(W_{3,j} - W_{1,j})) \\ &+ tr(\Lambda_2^T(W_{3,j} - W_{2,j})) + \frac{u_1}{2}||W_{3,j} - W_{1,j}||_F^2 + \frac{u_2}{2}||W_{3,j} - W_{2,j}||_F^2\end{aligned} \tag{15}$$

Solving the optimization problem (15), we update $W_{3,j}$ by:

$$\begin{aligned}W_{3,j} =&(\phi(Y_j^D)^T\phi(Y_j^D) + (u_1 + u_2)I)^{-1}Z \\ =&(K_{Y_j^D Y_j^D} - (u_1 + u_2)I)^{-1}Z\end{aligned} \tag{16}$$

where I is an identity matrix and the matrix Z is represented as:

$$\begin{aligned}Z =&\phi(Y_j^D)^T\phi(Y_j^A) + u_1W_{1,j} - \Lambda_1 + u_2W_{2,j} - \Lambda_2 \\ =&K_{Y_j^D Y_j^A} - u_1W_{1,j} + \Lambda_1 - u_2W_{2,j} + \Lambda_2\end{aligned} \tag{17}$$

Update multipliers

$$\begin{aligned}\Lambda_1 = \Lambda_1 + u_1(W_{3,j} - W_{1,j}); \Lambda_2=&\Lambda_2 + u_2(W_{3,j} - W_{2,j}) \\ u_1 = \rho u_1; u_2 =& \rho u_2\end{aligned} \tag{18}$$

where $\rho > 1$ is a scalar constant.

When the changes of objective variables during updates are below a defined threshold e, the optimization reaches convergence. We summarize this optimization in Algorithm 1.

Algorithm 1 Optimization of Kernel Based Low-rank Sparse Coding Problem

Input: Data Y_j^A, Sub-dictionary Y_j^D and parameters λ_1, λ_2, Λ_1, Λ_2, u_1 and u_2

while not converged **do**:

Fix the others and update $W_{1,j}$

$W_{1,j} = S_{\frac{\lambda_1}{u_1}}(W_{3,j} + \frac{1}{u_1}\Lambda_1)$

Fix the others and update $W_{2,j}$

$W_{2,j} = \Im_{\frac{\lambda_2}{u_2}}(W_{3,j} + \frac{1}{u_2}\Lambda_2)$

Fix the others and update $W_{3,j}$

$W_{3,j} = (K_{Y_j^D Y_j^D} - u_1\mathrm{I} - u_2\mathrm{I})^{-1}(K_{Y_j^D Y_j^A} - u_1 W_{1,j} + \Lambda_1 - u_2 W_{2,j} + \Lambda_2)$

Fix the others and update the multipliers Λ_1,Λ_2,u_1 and u_2

$\Lambda_1 = \Lambda_1 + u_1(W_{3,j} - W_{1,j}); \Lambda_2 = \Lambda_2 + u_2(W_{3,j} - W_{2,j})$

$u_1 = \rho u_1; u_2 = \rho u_2$

end while

Output: $W_{3,j}$

2.3.3. Effectiveness of KLRSC

To explain the effectiveness of KLRSC, we perform an experiment to investigate the statistical property of sparse coding noises (SCN) for different coding methods. We use *lena* image as a test image. Its LR counterpart is generated through blurring (Gaussian kernel with standard deviation 1.6), down-sampling and up-scaling (with a factor of 1.25). We collect 15625 pairs of LR and HR features from the LR and HR images. DCT dictionary is used in our experiment. We denote method of sparse coding with low-rank constraint as 'LRSC' which appeared in our preliminary work [14]. We firstly calculate the sparse coefficients for them using KLRSC, LRSC and SC, respectively. We calculate SCN by following the definition in [13]. In our experiment, We evaluate SCN

by $\ell 2$ norm. In Fig 4, we draw the $\ell 2$ norm distributions of SCN for KLRSC, LRSC and conventional SC. The distribution for KLRSC, LRSC and SC is drawn in red, blue and black lines, respectively. It is shown that KLRSC get lower SCN than the other two methods do, which means that the proposed KLRSC approach effectively suppress SCN utilizing the low-rank property of nonlocal-similarity and improve the coding performance.

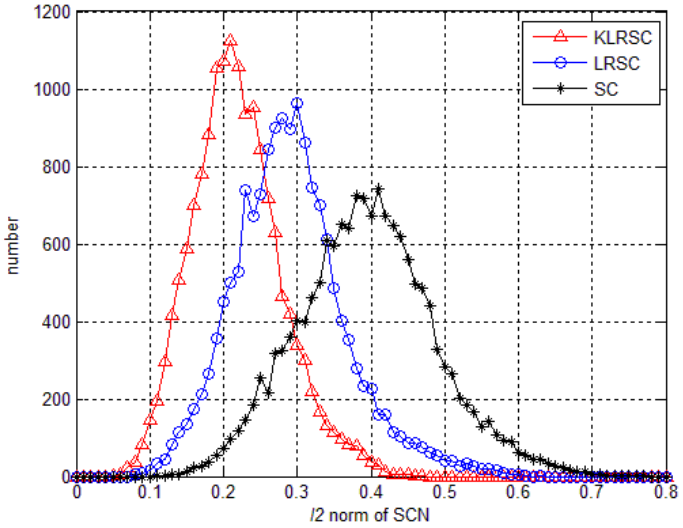

Figure 4: $\ell 2$ norm distributions of SCN for KLRSC, LRSC and SC.

2.3.4. Post-processing procedure

When the optimization converges, the solution $W_{3,j}$ becomes both sparse and low-rank. Then we distil the first column of $W_{3,j}$ as the sparse weight w_j^{lr} for the reconstruction of the HR patch x_j because low-rank constraint does not change the identities of columns. The HR patch x_j can be sparsely represented upon X_j^D as:

$$x_j = X_j^D w_j^{lr} \cdot ||l_j||_2 + \bar{l} \tag{19}$$

where $||l_j||_2$ is the $\ell 2$-norm of the corresponding LR feature and $\bar{l}$ denotes the average intensity of the corresponding LR patch. Having obtained all HR patches

$X_i = \{x_j\}_i$, we merge them into the layer I_i by averaging the intensity of the overlapping pixels between the adjacent patches.

To enhance quality of the reconstructed interim layer, we apply IBP algorithm [5] and pixel-wise autoregressive (AR) model [17] to both enforce the global reconstruction constraint between the interim layer and the input I_0 and refine the relation between neighboring pixels.

The j-th pixel of the reconstructed layer is expected to be predicted as a linear combination of its neighboring pixels in a 3×3 square window: $s_j = a_j^T q_j$, where s_j is the central pixel and q_j is the vector consisting of its neighbors. To learn the combination weights a_j, we collect the N nearest neighbors of the s_j centered patch from other already reconstructed HR layers. These patches are assumed to share the same neighboring relationship. The combination weights a_j can be obtained by the following optimization problem:

$$a_j = \arg\min_{a_j} \sum_{n=1}^{N} (s_j^n - a_j^T q_j^n)^2 + \eta ||a_j||_2^2 \tag{20}$$

a_j can be derived by:

$$a_j = (QQ^T + \eta E)^{-1} QS^T \tag{21}$$

where $Q = [q_j^1, q_j^2, ..., q_j^N]$, $S = [s_j^1, s_j^2, ..., s_j^N]$ and E is the identity matrix. Thus, we regularize the estimated layer by minimize the AR prediction error and the global reconstruction error by:

$$I_i^* = \arg\min_{I_i} ||I_0 - D_i B_i I_i||_F^2 + \alpha ||I_i - A_i I_i||_F^2 + \beta ||I_i - I_{i,0}||_F^2 \tag{22}$$

where A_i describes pixel-wise relationships in I_i, $I_{i,0}$ denotes the initial HR estimation, I_0 is the LR observation, D_i and B_i are the down-sampling and blurring operator of the i-th layer, respectively. The layer I_i is updated by:

$$I_{i,t+1} = I_{i,t} + \tau[B_i^T D_i^T (I_0 - D_i B_i I_{i,t}) - \alpha (E - A_i)^T (E - A_i) I_{i,t} - \beta (I_{i,t} - I_{i,0})] \tag{23}$$

where τ is the step size for gradient descent.

According to the self-similarity learning framework, we repeat the aforementioned low-rank sparse representation based SR for N_U times followed by a fine adjustment to get the final SR result.

2.4. Summary

The complete SR process is summarized in Algorithm 2.

Algorithm 2 Proposed Kernel Based Low-Rank Sparse Model for Single Image Super-Resolution

---

Input: LR image $I_L(I_0)$ and up-scaling factor p

1: **Initialization**

Set the input image I_L as initial layer I_0. Create the double pyramids from the input image using (1) and (3). Collect self-examples from the pyramids to generate the LR dictionary L and the HR dictionary H

2: **Upscaling**

Gradual magnification loop:

for $i = 1$ to N_U do

1) Enlarge the last layer I_{i-1} by a factor of s to build the layer $U(I_i) \leftarrow (I_{i-1})_{\uparrow s}$.

2) Partition the layer $U(I_i)$ into LR patches $Y_i = \{y_j\}_i$.

3) Compute the kernel based low-rank sparse representation coefficients of each LR patch y_j.

4) Reconstruct the HR patch x_j

5) Merge the HR patches $\{x_j\}_i$ into the layer I_i.

6) Refine the layer I_i by IBP and AR using (23).

end for

3: **Image size adjustment**

Down-sample the final layer I_{N_U} to get I_H.

Output: HR image I_H

---

3. Experimental results

In our experiments, we use nine test images from the software package for [17]. These images (see Fig. 5) cover various contents including humans, animals, plants and man-made objects. The size of image *parthenon* is 459×292 and the size of other images is 256×256. We compare our method with SC-SR [7], ASDS [17], LRNE-SR [32], DM-SR [12], NCSR [13] and Aplus [33]. Since the human visual systems are more sensitive to luminance changes in color images, we only perform our proposed method on the luminance component. The SR performances are evaluated in the luminance channel by the peak signal-to-noise ratio (PSNR) and the structural similarity (SSIM) [34] objectively.

Figure 5: Test Images

3.1. Experimental setting

The color test images are blurred with 7×7 Gaussian kernel with standard variation $\sigma = 1.6$ and then down-sampled by bicubic interpolation to generate the LR input images. All the layers of images are split into 7×7 patches with overlap of five pixels. The number of layers of LR and HR pyramids to train the self-example dictionary is $N_D = 4$. The up-scaling factor for each time of magnification is $s = 1.25$. The standard variance of Gaussian Blur kernel for the generation of the n-th layer I_{-n} is computed by (2). The number of the neighbors for low-rank sparse representation K_D is 60. The number of similar nonlocal neighbors K_N is 20. We set $\lambda_1 = 0.07$, $\lambda_2 = 0.07$, $\rho = 1.5$. We obtain initialization of codes Z_0 by standard sparse coding [7] and let $Z_1 = Z_2 = Z_3 = Z_0$ at the beginning of optimization. We set $u_1 = 1/max(\Sigma(Z_0))$ and $u_2 = 1/||Z_0||_\infty$. For the stage of IBP and AR regularization, the window size is 3×3. The maximum iteration times is set to 300. We set the step size $\tau = 0.5$. The parameters α and β are set to 0.05 and 0.01.

For fairness of the comparisons, according to the experimental setting, we retrain the LR-HR dictionary for [7] and [32] and change all down-sampling and up-scaling for [13] and [17] to bicubic and retrain its AR models and nonlocal adaptive regularization models before implementation.

3.2. Experimental results

The PSNRs and SSIMs of different methods for comparisons are shown in Table 1 for the scaling factor $p = 3$ and Table 2 for the scaling factor $p = 4$, respectively. Our proposed method gets better quantitative SR performances on most of the test images than other methods. The average gains of our proposed method for the scaling factor $p = 3$ over the second best method are 0.293dB in PSNR and 0.0078 in SSIM. In the case of $p = 4$, the average gains are 0.420dB in PSNR and 0.0117 in SSIM.

Fig. 6-8 show the visual SR results in the case of $p = 3$ on the images *girl butterfly* and *hat* by different methods, respectively. Fig. 9-11 show the visual SR results of the same test images with the factor of $p = 4$. The SC-SR

Table 1: PSNRs (dB) and SSIMs by different SR methods with the scaling factor $p = 3$ ($\sigma = 1.6$)

Image	Bi-cubic	SC-SR[7]	ASDS [17]	LRNE-SR[32]	DM-SR[12]	NCSR [13]	Aplus [33]	Pro-posed
Lena	29.600	30.489	31.232	30.618	30.691	31.357	31.610	**31.884**
	0.8306	0.8556	0.8693	0.8523	0.8555	0.8747	0.8708	**0.8791**
Girl	32.724	33.529	33.753	33.422	33.599	33.982	33.367	**34.319**
	0.8162	0.8386	0.8417	0.8321	0.8410	0.8489	0.8205	**0.8540**
Butt-erfly	23.103	24.337	25.196	24.815	24.940	25.391	**26.808**	26.735
	0.7926	0.8375	0.8680	0.8553	0.8615	0.8754	0.8980	**0.9003**
Parrot	27.406	28.488	29.309	28.339	28.728	29.355	29.460	**29.503**
	0.8692	0.8910	0.9025	0.8876	0.8932	0.9063	0.9049	**0.9087**
Flower	26.935	27.949	28.489	27.885	28.177	28.581	28.802	**29.230**
	0.7594	0.8025	0.8215	0.7978	0.8113	0.8285	0.8382	**0.8437**
Pepper	27.269	28.275	29.065	28.605	28.527	29.140	29.514	**30.059**
	0.8393	0.8628	0.8827	0.8697	0.8704	0.8862	0.8764	**0.8967**
Bike	22.502	23.385	23.928	23.407	23.555	24.010	24.264	**24.429**
	0.6640	0.7235	0.7494	0.7177	0.7313	0.7563	**0.7782**	0.7721
Hat	28.958	29.824	30.363	30.030	30.107	30.530	30.915	**31.177**
	0.8233	0.8454	0.8568	0.8508	0.8536	0.8641	0.8670	**0.8739**
Parth-enon	25.593	26.081	26.543	26.137	26.228	26.608	26.823	**26.869**
	0.6683	0.6978	0.7118	0.6923	0.6992	0.7180	**0.7315**	0.7266
Avg.	27.121	28.040	28.653	28.140	28.284	28.773	29.063	**29.356**
	0.7848	0.8172	0.8337	0.8173	0.8241	0.8398	0.8428	**0.8506**

method [7] generates blurry along edges (i.e., the boundary of the girl's nose) because the single over-complete dictionary learned from the external training images is not prone to produce sharp edges. LRNE-SR [32] tends to lose high-frequency details while smooth regions and clean edges are produced. As one of the state-of-the-art methods for image SR, Aplus [33] obtains the second best quantitative SR performances (see Table 1 and 2), however, too sharp boundaries and ringing artifacts can also be observed. Our proposed method

Table 2: PSNRs (dB) and SSIMs by different SR methods with the scaling factor $p = 4$ ($\sigma = 1.6$)

Image	Bi-cubic	SC-SR[7]	ASDS [17]	LRNE-SR[32]	DM-SR[12]	NCSR [13]	Aplus [33]	Pro-posed
Lena	27.820	28.529	29.254	28.591	29.039	29.908	29.610	**30.083**
	0.7605	0.7849	0.8047	0.7838	0.8000	0.8234	0.8204	**0.8252**
Girl	31.263	31.814	32.211	31.826	32.211	32.109	31.971	**32.635**
	0.7601	0.7768	0.7873	0.7743	0.7885	0.7751	0.7699	**0.7978**
Butt-erfly	21.438	22.656	23.666	22.737	23.781	24.208	23.996	**24.827**
	0.7121	0.7555	0.8145	0.7721	0.8198	0.8295	0.8316	**0.8511**
Parrot	25.512	26.416	26.966	26.276	26.796	**27.428**	27.228	27.183
	0.8145	0.8380	0.8521	0.8346	0.8486	**0.8654**	0.8638	0.8639
Flower	25.259	26.113	26.452	25.952	26.510	26.850	26.706	**27.022**
	0.6689	0.7157	0.7306	0.7071	0.7366	0.7552	0.7498	**0.7597**
Pepper	25.527	26.358	27.153	26.480	27.011	27.668	27.367	**27.887**
	0.7660	0.7866	0.8174	0.7925	0.8135	0.8296	0.8279	**0.8340**
Bike	21.021	21.747	22.248	21.738	22.172	22.646	22.423	**22.716**
	0.5585	0.6170	0.6488	0.6108	0.6462	0.6774	0.6673	**0.6800**
Hat	27.487	28.187	28.699	28.344	26.510	29.347	29.022	**29.485**
	0.7771	0.7933	0.8108	0.8009	0.7366	0.8277	0.8226	**0.8319**
Parth-enon	24.875	25.388	25.682	25.366	25.628	25.549	25.516	**25.783**
	0.6296	0.6574	0.6683	0.6518	0.6659	0.6620	0.6593	**0.6748**
Avg.	25.578	26.356	26.926	26.368	26.629	27.301	27.093	**27.513**
	0.7163	0.7472	0.7705	0.7476	0.7617	0.7828	0.7792	**0.7909**

generates obvious boundaries and suppresses artifacts. We can see clear edges of girls nose and natural patterns in the wing of butterfly. As seen from the visual experimental results, our proposed method gets better results than other methods perceptually.

3.3. Evaluation of the different contributions

To further validate the effectiveness of proposed method, we test the SR performances with the scaling factor $p = 3$ using sparse coding with differ-

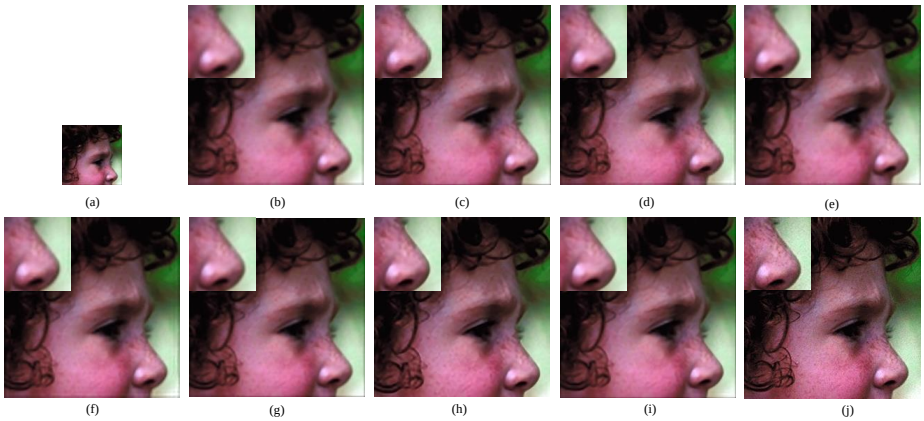

Figure 6: Visual results comparison for image *girl* ($\times 3$, $\sigma = 1.6$). (a)LR input. (b)bicubic. (c)SC-SR[7]. (d)ASDS[17]. (e)LRNE-SR[32]. (f)DM-SR[12]. (g)NCSR[13]. (h)Aplus[33]. (i)proposed method. (j)ground truth.

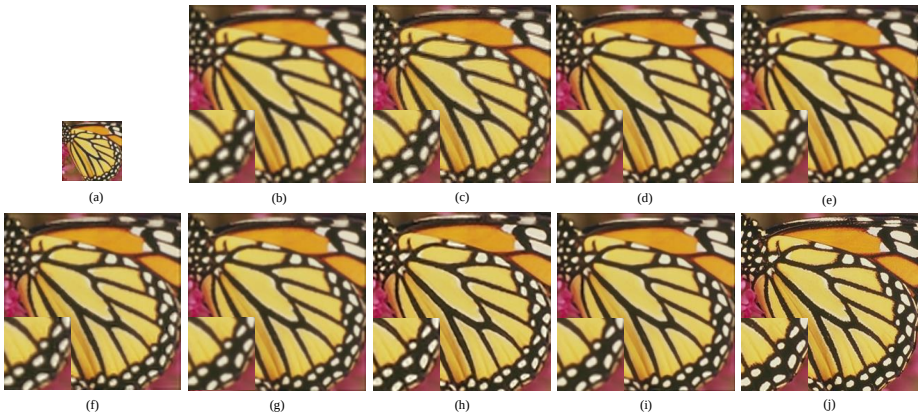

Figure 7: Visual results comparison for image *butterfly* ($\times 3$, $\sigma = 1.6$). (a)LR input. (b)bicubic. (c)SC-SR[7]. (d)ASDS[17]. (e)LRNE-SR[32]. (f)DM-SR[12]. (g)NCSR[13]. (h)Aplus[33]. (i)proposed method. (j)ground truth.

ent constraints and regularization. The results are shown in Fig. 12. For the convenience of description, we denote sparse coding as 'SC', sparse coding with low-rank constraint as 'LRSC' and autoregressive as 'AR'. Our proposed KLRSC incorporated with AR model gains the highest PSNRs and SSIMs for all the reconstructions of images. Table 3 shows the average SR performance using SC, LRSC, KLRSC and KLRSC+AR. The proposed KLRSC+AR method

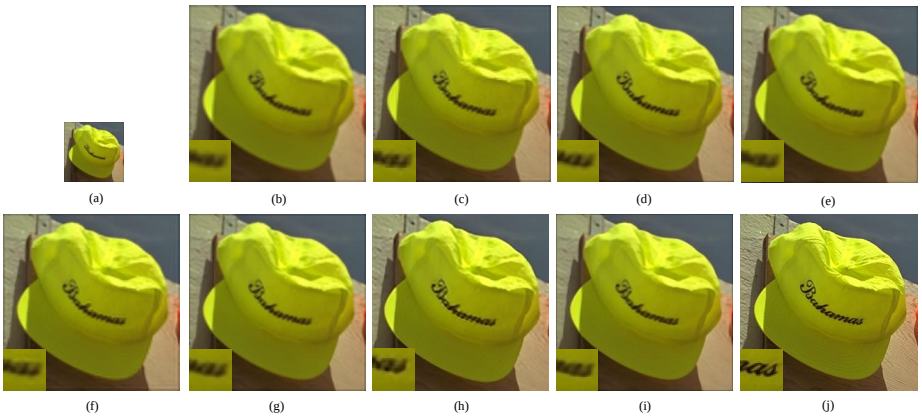

Figure 8: Visual results comparison for image *hat* ($\times 3$, $\sigma = 1.6$). (a)LR input. (b)bicubic. (c)SC-SR[7]. (d)ASDS[17]. (e)LRNE-SR[32]. (f)DM-SR[12]. (g)NCSR[13]. (h)Aplus[33]. (i)proposed method. (j)ground truth.

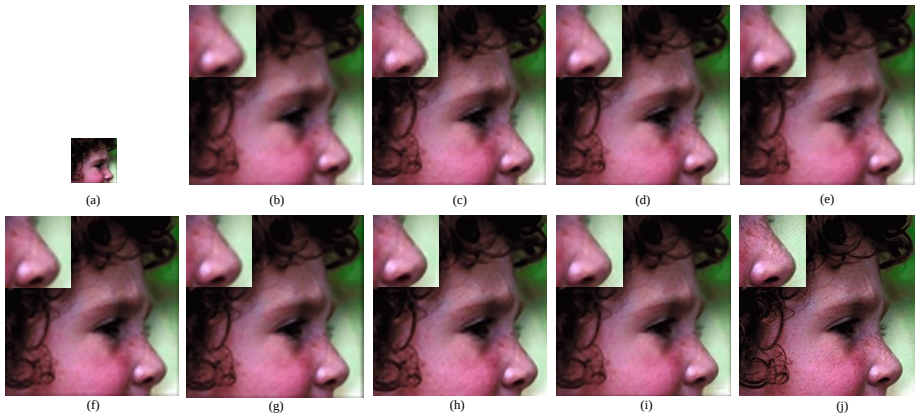

Figure 9: Visual results comparison for image *girl* ($\times 4$, $\sigma = 1.6$). (a)LR input. (b)bicubic. (c)SC-SR[7]. (d)ASDS[17]. (e)LRNE-SR[32]. (f)DM-SR[12]. (g)NCSR[13]. (h)Aplus[33]. (i)proposed method. (j)ground truth.

has an average improvement of 0.664dB in PSNR and 0.0148 in SSIM over the method using standard sparse representation, where the average PSNR/SSIM contributions of the low-rank constraint, the kernel method and the AR regularization are 0.120dB/0.0028, 0.284dB/0.0041 and 0.260dB/0.0079, respectively. It indicates that the incorporation of low-rank constraint, kernel method and AR regularization indeed boosts the SR results.

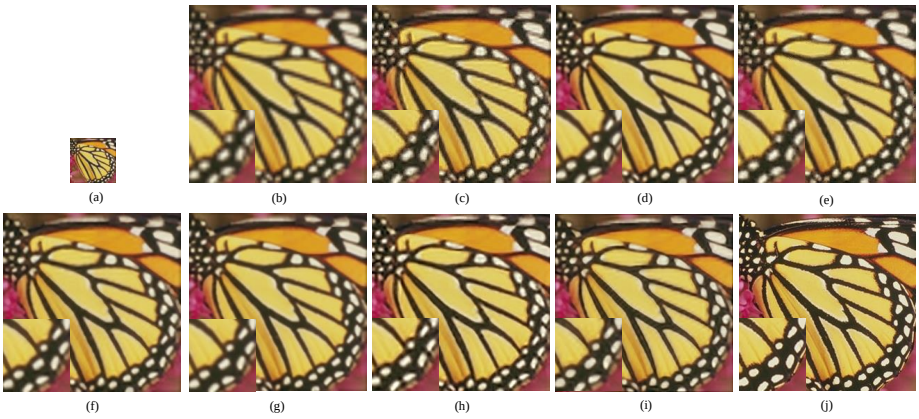

Figure 10: Visual results comparison for image *butterfly* ($\times 4$, $\sigma = 1.6$). (a)LR input. (b)bicubic. (c)SC-SR[7]. (d)ASDS[17]. (e)LRNE-SR[32]. (f)DM-SR[12]. (g)NCSR[13]. (h)Aplus[33]. (i)proposed method. (j)ground truth.

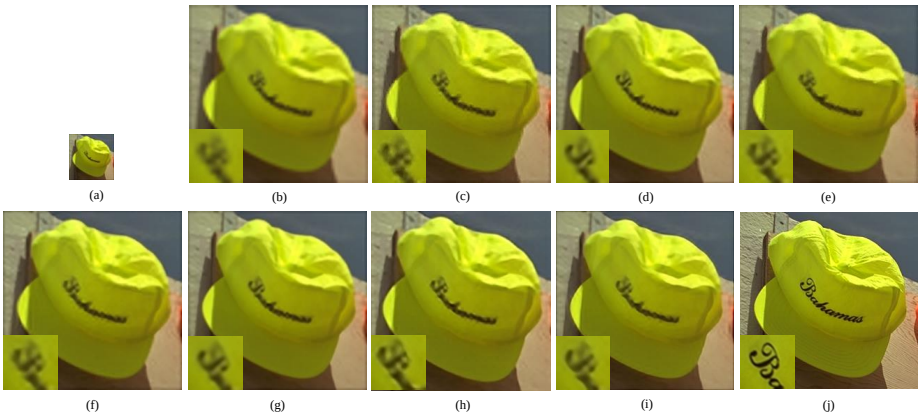

Figure 11: Visual results comparison for image *hat* ($\times 4$, $\sigma = 1.6$). (a)LR input. (b)bicubic. (c)SC-SR[7]. (d)ASDS[17]. (e)LRNE-SR[32]. (f)DM-SR[12]. (g)NCSR[13]. (h)Aplus[33]. (i)proposed method. (j)ground truth.

Table 3: The average SR performance using SC, LRSC, KLRSC and KLRSC+AR.

	SC		LRSC		KLRSC		proposed KLRSC+AR	
	PSNR	SSIM	PSNR	SSIM	PSNR	SSIM	PSNR	SSIM
Avg.	28.692	0.8358	28.812	0.8386	29.096	0.8427	**29.356**	**0.8506**

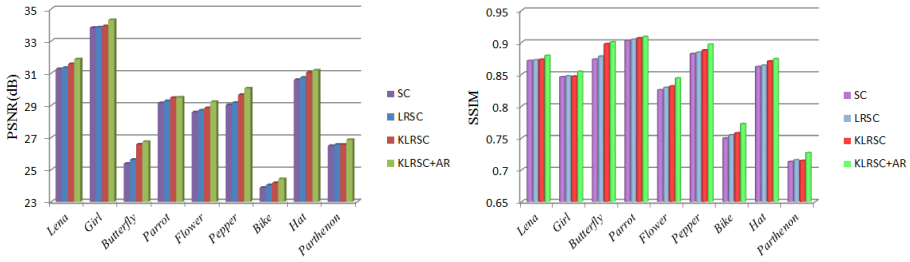

Figure 12: SR performances with the scaling factor 3 using sparse coding with different constraints and regularization.

4. Conclusion

In this paper, we propose a novel single image SR method by incorporating self-similarity learning framework with kernel based low-rank sparse coding. The kernel method is used which captures the nonlinear structures of the input data. A novel kernel based low-rank sparse coding based scheme for single image SR is proposed, which exploits both the structural information of nonlocal-similarity in kernel space. Furthermore, we exploit the self-similarity redundancy among patches across different scales in a single natural image to train a self-example dictionary. The gradual magnification framework compatible to the self-example dictionary is adopted. Experimental results demonstrate that our proposed method improves SR performances both quantitatively and perceptually.

References

References

[1] J. Sun, J. Sun, Z. Xu, H.-Y. Shum, Gradient profile prior and its applications in image super-resolution and enhancement, IEEE Transactions on Image Processing 20 (2011) 1529–1542. doi:10.1109/TIP.2010.2095871.

[2] Y. Ogawa, Y. Ariki, T. Takiguchi, Super-resolution by gmm based conversion using self-reduction image 22 (10) (2012) 1285–1288. doi:10.1109/ICASSP.2012.6288124.

[3] C. V. Jiji, M. V. Joshi, S. Chaudhuri, Single-frame image super-resolution using learned wavelet coefficients, International Journal of Imaging Systems and Technology 14 (14) (2004) 105–112. doi:10.1002/ima.20013.

[4] A. Marquina, S. J. Osher, Image super-resolution by tv-regularization and bregman iteration, J. Sci. Comput. 37 (2008) 367–382. doi:10.1007/s10915-008-9214-8.

[5] M. Irani, S. Peleg, Motion analysis for image enhancement: resolution, occlusion, and transparency, J. Vis. Commun. Image Represent. 4 (1993) 324–335. doi:10.1006/jvci.1993.1030.

[6] H. Chang, D.-Y. Yeung, Y. Xiong, Super-resolution through a neighbor embedding, in: IEEE Conference on Computer Vision and Pattern Recognition, 2004, pp. 275–282. doi:10.1109/CVPR.2004.243.

[7] J. Yang, J. Wright, T. Huang, Y. Ma, Image super-resolution via sparse representation, IEEE Transactions on Image Processing 19 (2010) 2861–2873. doi:10.1109/TIP.2010.2050625.

[8] X. Ma, J. Zhang, C. Qi, Hallucinating face by position-patch, Pattern Recognition 43 (6) (2010) 2224–2236. doi:10.1016/j.patcog.2009.12.019.

[9] D. Glasner, S. Bagon, M. Irani, Super-resolution from a single image, in: IEEE International Conference on Computer Vision, 2009, pp. 349–356. doi:10.1109/ICCV.2009.5459271.

[10] K. Zhang, X. Gao, D. Tao, X. Li, Single image super-resolution with multiscale similarity learning, IEEE Transactions on Neural Networks and Learning Systems 24 (10) (2013) 1648–1659. doi:10.1109/TNNLS.2013.2262001.

[11] J. Yu, X. Gao, D. Tao, X. Li, K. Zhang, A unified learning framework for single image super-resolution, IEEE Transactions on Neural Networks and Learning Systems 25 (2014) 780–792. doi:10.1109/TIP.2010.2050625.

[12] M. Bevilacqua, A. Roumy, C. Guillemot, M.-L. Morel, Single-image super-resolution via linear mapping of interpolated self-examples, IEEE Transactions on Image Processing 23 (2014) 5334–5347. doi:10.1109/TIP.2014.2364116.

[13] W. Dong, L. Zhang, G. Shi, X. Wu, Nonlocally centralized sparse representation for image restoration, IEEE Transactions on Image Processing 20 (2011) 1838–1857. doi:10.1109/TIP.2012.2235847.

[14] J. Shi, C. Qi, Low-rank sparse representation for single image super-resolution via self-similarity learning, in: IEEE International Conference on Image Processing, 2016, pp. 1424–1428. doi:10.1109/ICIP.2016.7532593.

[15] B. Schölkopf, A. Smola, K.-R. Müller, Kernel principal component analysis, in: International Conference on Artificial Neural Networks, 1997, pp. 583–588. doi:10.1007/BFb0020217.

[16] C.-Y. Yang, J.-B. Huang, M.-H. Yang, Exploiting self-similarities for single frame super-resolution, in: Asian Conference on Computer Vision, 2010, pp. 497–510. doi:10.1007/978-3-642-19318-7_39.

[17] W. Dong, L. Zhang, G. Shi, X. Wu, Image deblurring and super-resolution by adaptive sparse domain selection and adaptive regularization, IEEE Transactions on Image Processing 20 (2011) 1838–1857. doi:10.1109/TIP.2011.2108306.

[18] J. Lu, H. Zhang, Y. Sun, Video super resolution based on non-local regularization and reliable motion estimation, Signal Processing: Image Communication 29 (4) (2014) 514 – 529. doi:http://dx.doi.org/10.1016/j.image.2014.01.002.

[19] J. Mairal, F. Bach, J. Ponce, G. Sapiro, A. Zisserman, Non-local sparse models for image restoration, in: IEEE International Conference on Computer Vision, 2009, pp. 2272–2279. doi:10.1109/ICCV.2009.5459452.

[20] H. Chen, X. He, Q. Teng, C. Ren, Single image super resolution using local smoothness and nonlocal self-similarity priors, Signal Processing: Image Communication 43 (2016) 68 – 81. doi:http://dx.doi.org/10.1016/j.image.2016.01.007.

[21] T. Zhang, B. Ghanem, S. Liu, C. Xu, N. Ahuja, Low-rank sparse coding for image classification, in: IEEE International Conference on Computer Vision, 2013, pp. 281–288. doi:10.1109/ICCV.2013.42.

[22] B. Recht, M. Fazel, P. A. Parrilo, Guaranteed minimum-rank solutions of linear matrix equations via nuclear norm minimization, SIAM Review 52 (3) (2010) 471–501. doi:10.1137/070697835.

[23] E. J. Candes, X. D. Li, Y. Ma, J. Wright, Robust principal component analysis?, Journal of the ACM 58 (2011) 11:1–11:37. doi:10.1145/1970392.1970395.

[24] X. Liu, G. Zhao, J. Yao, C. Qi, Background subtraction based on low-rank and structured sparse decomposition, IEEE Transactions on Image Processing 24 (2015) 2502–2514. doi:10.1109/TIP.2015.2419084.

[25] Z. Zhang, A. Ganesh, X. Liang, Y. Ma, Tilt: Transform invariant low-rank textures, International Journal of Computer Vision 99 (2012) 1–24. doi:10.1007/s11263-012-0515-x.

[26] Y. Tang, Y. Yuan, Learning from errors in super-resolution, IEEE Transactions on Cybernetics 44 (2014) 2143–2154. doi:10.1109/TCYB.2014.2301732.

[27] K. Ren, F. Xu, Super-resolution images fusion via compressed sensing and low-rank matrix decomposition, Infrared Physics and Technology 68 (2015) 61–68. doi:10.1016/j.infrared.2014.11.006.

[28] S. Wang, S. Lin, X. Liang, B. Yue, L. Jiao, External and internal learning for single-image super-resolution, in: IEEE International Conference on Image Processing, 2015, pp. 128–132. doi:10.1109/ICIP.2015.7350773.

[29] S. Gao, I. W.-H. Tsang, L.-T. Chia, Kernel sparse representation for image classification and face recognition, in: European Conference on Computer Vision, Heraklion, 2010, pp. 1–14. doi:10.1007/978-3-642-15561-1_1.

[30] J. Shi, C. Qi, Kernel-based face hallucination via dual regularization priors, IEEE Signal Processing Letters 22 (8) (2015) 1189–1193. doi:10.1109/LSP.2015.2390972.

[31] Z. Lin, A. Ganesh, J. Wright, L.Wu, M. Chen, Y. Ma, Fast convex optimization algorithms for exact recovery of a corrupted low-rank matrix, in: Technical Report UILU-ENG-09-2214, 2009.

[32] X. Chen, C. Qi, Low-rank neighbor embedding for single image super-resolution, IEEE Signal Processing Letters 21 (2014) 79–82. doi:10.1109/LSP.2013.2286417.

[33] R. Timofte, V. DeSmet, V. Luc, A+: Adjusted anchored neighborhood regression for fast super-resolution, in: Asian Conference on Computer Vision, 2015, pp. 111–126. doi:10.1007/978-3-319-16817-3_8.

[34] Z. Wang, A. C. Bovik, H. R. Sheikh, E. P. Simoncelli, Image quality assessment: from error visibility to structural similarity, IEEE Transactions on Image Processing 13 (4) (2004) 600–612. doi:10.1109/TIP.2003.819861.